

Biochemistry. Author manuscript; available in PMC 2014 July 30.

Published in final edited form as:

Biochemistry. 2013 July 30; 52(30): 5039-5050. doi:10.1021/bi4006946.

P450cin Active Site Water: Implications for Substrate Binding and Solvent Accessibility

Yarrow Madrona, **Scott A. Hollingsworth**, **Bushra Khan**, and **Thomas L. Poulos***

Departments of Molecular Biology and Biochemistry, Chemistry, and Pharmaceutical Sciences, University of California, Irvine, California 92697-3900

Abstract

In P450cin Tyr81, Asp241, Asp242, two water molecules, and the substrate participate in a complex H-bonded network. The role of this H-bonded network in substrate binding and catalysis has been probed by crystallography, spectroscopy, kinetics, isothermal titration calorimetry (ITC), and molecular dynamics. In the Y81F mutant the substrate binds about 20-fold more weakly than WT while Vmax decreases by about 30%. Enhanced susceptibility of the heme to H₂O₂ destruction in Y81F suggests that this mutant favors the open, low-spin conformational state. Asn242 H-bonds directly with the substrate and replacing the former with Ala results in water taking the place of the missing Asn side chain. This mutant exhibits a 70% decrease in activity. Crystal structures and molecular dynamics simulations of substrate bound complexes show that solvent has more ready access to the active site, especially in the N242A mutant. This accounts for about 64% uncoupling of electron transfer from substrate hydroxylation. These data indicate the importance of the interconnected water network on substrate binding and the on the open/close conformational equilibrium both of which are critically important for maintaining high coupling efficiency.

Cytochrome P450 enzymes (CYPs) catalyze the oxidation of a diverse range of compounds including xenobiotics, steroids, and in some bacteria, compounds that are oxidatively assimilated as energy sources using the following reaction.

$$R - H + NADPH + O_2 + H^+ \rightarrow R - OH + NADP^+ + H_2O$$

NADPH or NADH provides two electrons that are sequentially transferred to the heme iron to activate molecular dioxygen and ultimately hydroxylate the subtrate. P450 enzymes exhibit varying levels of 'uncoupling' producing hydrogen peroxide or water instead of hydroxylated product. However, tightly controlled P450 enzymes have precise water-mediated H-bonding networks that ensure proper dioxygen protonation. Disrupting this network can lead to nonspecific delivery of protons that uncouple NADPH consumption from substrate hydroxylation. Much of the earlier proposals on the O_2 activation process were based on P450 structures in the so-called closed state. However, it is now clear that key elements of the O_2 activation machinery show much more conformational freedom than could be seen in early substrate-bound crystal structures. A recent P450cam substrate-free structure¹ as well as intermediate structures of substrate analog tethered linkers² show dynamic retractions of the F and G helices and B-C loops in the absence of substrate. The

^{*}Corresponding author: poulos@uci.edu; 949-824-7020.

[‡]Coordinates and structure factors have been deposited in the Protein Data Bank under accession numbers 4LHT, 4L6G and 4L77. Supporting Information: Figures S1, S2, and S3 are available free of charge via the Internet at http://pubs.acs.org.

open/close transition has also been studied in solution using spectroscopic methods such as DEER³ and NMR⁴. This kind of flexibility is likely to be important in oxygen activation in P450cam^{5,6} and we have postulated that similar motions are important when comparing the P450cin substrate bound and substrate-free structures (Fig. 1).⁷

P450cam, the active site is not surrounded by a wall of nonpolar residues but instead an intricate lattice of water bridged hydrogen bonds. This water network involves Tyr81, Asn242, and Asp241 (Fig. 2). The roles of Asn242 and Asp241 have been analyzed by mutagenesis, but the role of Tyr81 has not been explored. In addition, crystallographic data on these various mutants are limited. To further probe the unique water network in P450cin we have analyzed the Y81F and N242A mutants using crystallography, enzyme kinetics, titration calorimetry, and molecular dynamics.

Materials and Methods

Site Directed Mutagenesis

The PcW-P450cin expression plasmid with amino acids 2-7 deleted was provided by Prof. James De Voss. The Y81F and N242A mutants were cloned with overlapping complimentary primers using a modification of the Invitrogen® QuickChange site directed mutagenesis protocol. Mutagenic primers are listed below with mutated bases in bold: Y81F(f); GTG ACC TTC CCT CGC TTC GAA ACC GGC GAG TTC G; Y81F(r): C GAA CTC GCC GGT TTC GAA GCG AGG GAA GGT CAC; N242A(f):GCT TCT CGG CGG CAT CGA CGC CAC CGC ACG CTT CCT CAG; N242A(r): CTG AGG AAG CGT GCG GTG GCG TCG ATG CCG CCG AGA AGC. Each PCR reaction was split into two aliquots containing forward and reverse primers. Three PCR cycles with an annealing temperature of 59 °C was initiated for each aliquot. The reverse and forward reactions were then combined followed by 18 PCR cycles with an annealing temperature of 59 °C. *DPN*1 enzyme was added to the PCR reactions and incubated for 5 hours at 37 degrees followed by chemical transformation into DH5 *E. coli* and plated overnight at 37 degrees on Luria-Bertani broth agar plates containing 100ug/mL ampicillin. Plasmids were then prepared from overnight cultures and sequenced.

Catalytic activity - NADPH Turnover

All activity assays were executed on a Cary 3E UV-visible spectrophotometer at room temperature. Catalytic rates were determined by using an established reconstituted turnover assay in which the native cindoxin reductase enzyme was replaced by *E.coli* flavodoxin reductase (Fpr). NADPH provides reducing equivalents to Fpr for sequential electron shuttling to cindoxin (Cdx) and then to P450cin to hydroxylate 1,8-cineole to 1(R)-6 - hydroxycineole. The reaction contained 700µl of 50mM Tris buffer, pH 7.8, Fpr (4µM), Cdx (4µM), P450cin (0.5µM), and 1,8-Cineole (200µM). Catalytic turnover was initiated by adding NADPH (400µM) and NADPH oxidation was determined from the loss of absorbance at 340nm. The rate of NADPH consumption, corrected for background NADPH oxidation, was determined by dividing the slope of the curve by the NADPH extinction coefficient of 6.22mM $^{-1}$ cm $^{-1.12}$ Reactions were incubated for 2 minutes producing a linear curve. k_{cat} was determined by dividing the rate of NADPH consumption by µmoles of P450cin used.

Product formation – GC-MS

NADPH driven catalytic turnover was initiated as described above. Samples taken at time intervals between 0-2 minutes were quenched and extracted with 700µl ethyl acetate. These samples were vortexed for 15 seconds followed by the addition of 4.6µl of 30µM camphor as an internal standard and vortexed for 1min. After centrifugation for 1min the organic

layer was removed for gas chromatography-mass spectrometry analysis on a Finnigan Trace GC 2000 (Thermoquest Instruments) fitted with a J&W DB-5 column, $30m \times 0.25$ mm id. (Agilent). Fig. S1 displays the total ion current at selected time points for the WT, Y81F and N242A mutants. The temperature was increased from 50-250 °C at a rate of 10 °C/min. A standard curve was generated by performing the same reaction in the absence of NADPH and adding known concentrations of cineole. All enzyme reactions were performed in triplicate. The ratio of the integrated peaks for cineole was divided by that of the internal standard and compared to the standard curve constructed from known cineole concentrations (Fig. S2). Cineole and camphor, purchased from Sigma-Aldrich at greater than 98% purity, were assigned to peaks in the mass spectra consistent with their molecular weights. Peaks for *gas chromatography-mass spectrometry m/z*, cineole: 154 (M⁺, 3.4%), 139 (M – CH₃), 108, 96, 93, 84, 81, 71, 69, 68, 58. Camphor: 152 (M⁺, 4.1%), 137 (M – CH₃), 108, 95, 83, 81, 69, 67, 55. A peak that increased upon assay time had a mass spectrum previously reported for hydroxycineole and its fragments 13 (gas chromatography-mass spectrometry m/z: $170(M^+, 0.62\%)$, 155 (M – CH₃), 126, 111, 108, 93, 71, 69).

1,8-Cineole Binding Spin Shift Assays

Difference spectroscopy was used to determine the spin shift binding constant, K_s , using previously published methods. ¹³ Assays were performed on a Cary 3E UV-visible spectrophotometer in the dual beam mode. Both the reference and sample cuvettes contained 1mL of 2 μ M P450cin diluted in 50mM Tris, pH 7.8. Samples contained increasing concentrations of cineole, diluted from a stock in the same buffer. K_s was determined by plotting the change in absorbance between high spin (392nm) and low spin (415nm) versus cineole concentration.

Isothermal Titration Calorimetry

Calorimetry measurements were performed on a VP-ITC titration calorimeter instrument from G.E Healthcare. Protein samples were exchanged into 50mM Tris, pH 7.8 by either gel filtration chromatography using Superdex 200 (G.E Life sciences) or by dialyzing in a 1/1000 ratio of buffer multiple times. All samples were extensively degassed under vacuum. Because the substrate is volatile, buffer was purged of oxygen by bubbling N2 and degassed under a vacuum manifold prior to dilution of substrate into buffer in a 1/600 ratio. The sample cell was filled with 220-290µM wild-type or N242A P450cin, whereas the Y81F mutant concentration was 430-450 µM. The injection syringe contained 10 mM cineole with all experiments performed in triplicate at 25 °C. Experiments were performed using 30-45 injections with a reference power of 10, a stirring speed of 307 RPM and a 150 second (WT/ N242A) or 240 second (Y81F) time delay between injections. Injection volumes for WT and the N242A mutants consisted of 3µl each. The injection volumes for the Y81F mutant were adjusted to 4µl for the first two and last four injections while all others were 15µl. The heats recorded were integrated and the data fit to a one-to-one binding mode. 14 Thermodynamic parameters were calculated with the Origin 7.0 graphing software. Standard deviations presented here are the result of three separate experiments and do not represent the standard deviations calculated from each individual curve fit.

Hydrogen peroxide-dependant heme depletion assays

Hydrogen peroxide-dependant heme depletion assays were performed as described previously 15 with the following changes. Hydrogen peroxide and P450cin were incubated in 50mM Tris, pH 7.4 buffer for two minutes with final concentrations of 100mM and 7 μ M, respectively. The loss of absorbance at 392nm (WT) or 416 (mutant and substrate-free) were measured in a Cary 3E UV-visible spectrophotometer at room temperature. The fraction remaining was calculated as the ratio of the current absorbance over the starting absorbance.

The assay was performed at increasing concentrations of cineole and the rate of degradation taken from the initial 30 seconds in which the slopes were linear.

Molecular dynamics simulations

The x-ray crystal structures solved herein were used as the starting configurations for each of the molecular dynamics simulations. Hydrogen atoms were added to both the protein and the crystallographic waters using psfgen with VMD 1.9.1 in preparation for the simulation. ¹⁶ To simulate bulk solvent, a water box with a 15Å cushion in x, y and z from the protein surface was added using VMD to generate the full system. The resulting systems of corresponding size and number of atoms were then ready for study: P450CIN WT (73.4 × 93.18 × 93.14, 57,680 atoms) and P450CIN N242A (99.0 × 93.0 × 83.0, 71,245 atoms). The difference in box size between the two systems was due to the protein being in different orientations with regards to the axis for each simulation.

All simulations were completed on Stampede (stampede.tacc.utexas.edu), using NAMD 2.9. ¹⁷ The CHARMM22 protein force field ¹⁸ was employed for all simulations as well as additional heme parameters available with the latest distribution of CHARMM force fields using the TIP3 water model. The cysteine-Fe (heme) bond was added with parameters from previous P450 simulations. ¹⁹ Simulations were carried out at a constant temperature utilizing a Langevin thermostat, ²⁰ the SHAKE algorithm²¹ to constrain bond lengths involving hydrogens and a time step of 1.0 femtosecond. The partial mesh Ewald method was implemented in the calculations of the Coulomb interactions. Each system was allowed to minimize for 1000 steps before the simulation was allowed to proceed. Simulations were carried out for a minimum of 75ns for each system and the resulting trajectories were analyzed on local systems using VMD, Caver3.0, ²² Fpocket, ²³ MDpocket, ²⁴ as well as locally developed analysis tools.

An additional force field was produced for cineole for these simulations. As cineole is very similar to the molecular structure of camphor which has previously been parameterized, the initial force field was based on a camphor force field developed previously. The cineoleunique bonds were then constructed from similar parameters released in the latest CHARMM force field release. The resulting force field then was compared to both the crystal structure and DFT calculations to ensure that there were no major penalties found in minimization, as well as a control force field generated using the generalized small molecule force field through Paramchem.org. ²⁶⁻²⁸ The resulting force field that was found to reflect accompanying DFT calculations (not shown) is included in the supplemental information (Fig.S3). The results were validated against previously obtained Amber force fields for cineole used in a separate simulation that further validated the obtained CHARMM cineole and protein force fields.

Caver and MD-pocket analysis

The resulting molecular dynamics trajectories were compressed, containing every 100th frame for an output rate of 100 ps/snapshot. Snapshots were converted to pdb files and fed into Caver3.0 and MD-pocket for analysis. For Caver, a shell radius of 3Å was used to define regions of bulk solvent, and a shell depth of 2Å was used to minimize superficial tunnels near the protein surface. The probe radius was set to 1.2Å and defines the minimum bottleneck radius a tunnel must exhibit to be identified. This probe radius was used for visualizing discrete tunnel pathways formed at some point in the simulation. In order to analyze the trend of a predominant tunnel over every snapshot it was necessary to use a probe radius smaller than the smallest tunnel radius for any given snapshot. Therefore, a 1.0Å probe radius was used for creating plots and tables that represent the single predominant tunnel present throughout the simulation. The starting point atoms from which

channels were probed in the N242A mutant were the Ala241 C atom, the Fe atom, and the cineole ethereal oxygen atom. Attempts were made to use similar starting points for WT, but because the active site is much tighter than the mutant, the starting point radius was smaller than the probe radius prohibiting tunnel visualization. Therefore, we chose the Leu237 C atom, the Fe atom, and the Asn242 C atom to define our WT starting radius. For MD-pocket analysis, the His 176 side-chain dihedral angle fluctuated between a cutoff of -180° and +180° making a plot in Cartesian coordinates misleading. We therefore wrapped the dihedral angle to produce continuous plots as described previously by Hollingsworth and Karplus. 29

Protein Characterization

P450cin WT and mutant protein preparations had an A_{280}/A_{415} ratio between 1.2-1.3 in the absence of substrate. Protein concentrations were determined by using the $_{415}$ of 150 mM $^{-1}$ cm $^{-1}$ for substrate free protein. 13 WT and mutant proteins exhibited a shift in absorbance to 450nm upon reduction and bubbling CO in excess substrate, characteristic of cytochrome P450 enzymes. Heme content was calculated to be >98% using the alkaline pyridine hemochromogen assay and an $_{\text{red}557} = 34.7 \text{ mM}^{-1} \text{ cm}^{-1}.^{30}$

P450cin Purification and Crystallization

WT and mutant P450cin was expressed and purified as previously described⁷ unless otherwise noted. The N242A and Y81F mutants were grown at 80 RPM and ambient temperature for 36 hours prior to harvesting. One hundred µM -aminolevulinic acid was added upon induction as well as after 18 hours. For the N242A mutant, initial crystals were grown from a 1:1 ratio of 1mM P450cin to well solution in sitting drop vapor diffusion CryschemTM crystal trays (15% PEG 3350, 100mM BisTris, pH 6.2, 150mM lithium sulfate, 3-5mM cineole, 0.2M TCEP-HCl, 100mM NaCl). For the Y81F mutant it was necessary to increase the cineole concentration to 7mM in order to obtain useable crystals although we were able to obtain a small handful of high quality crystals and one structure at 3mM cineole. For mutants, a two day incubation at room temperature produced crystals suitable for seeding. These crystals were then crushed to form a homogenous seed stock followed by serial dilution in mother liquor. Crystals were grown in mother liquor containing 12% PEG 3350 and streak seeded after a four hour incubation at room temperature. A five day incubation at room temperature yielded crystals of sufficient quality for x-ray data collection. These crystals were transferred into a mother liquor solution containing 15% PEG 3350 and increasing concentrations of PEG400 to a final concentration of 30% before flash cooling and storing in liquid nitrogen.

P450cin N242A and Y81F Data Collection and Refinement

X-ray diffraction data for the P450cin N242A and Y81F mutant crystallized in 7mM cineole were collected at the Stanford Synchrotron Radiation Light Source (Menlo Park, CA, USA) on beamline 9-2 using a Mar325 CCD detector. Diffraction Data for the Y81F mutant were collected at the Advanced Light Source (Berkeley, CA, USA) on beamline 8.2.1. In each case diffraction data were integrated using Mosflm³¹ and scaled using SCALA³² from the CCP4 suite.³³ For the N242A mutant, initial 2mFo-DFc and Fo-Fc maps were calculated with FFT from the CCP4 suite using phases taken from the wild-type crystal structure (PDB ID: IT2B). For the Y81F mutant, initial maps were determined by molecular replacement in phaser using wild-type as a starting model. Refinement was carried out in Phenix.refine from the Phenix package.³⁴ For the N242A and Y81F data sets, individual coordinates were refined as well as anisotropic B-factors. Iterative cycles of model improvement in Coot³⁵ followed by refinement resulted in our final refinement statistics (Table 1).

P450cin Y81F-3mM Cineole Data Collection and Refinement

Data for the Y81F mutant crystallized in 3mM cineole was collected on an in-house Rigaku Micromax 007HF rotating anode and a Saturn 944+ CCD detector. A stream of liquid nitrogen (Crystal Logic, Los Angeles, CA) kept the crystals at -160 C° during data collection. The crystal to detector distance was 100 mm and the 2 angle was -17°. The angle was incrementally increased by 0.5° with an exposure time of 45 seconds giving a total of 360 frames per data scan in angle. Two data scans were collected at angles of 15° and 30°. Diffraction data were integrated, merged and scaled using HKL2000.36 Initial 2mFo-DFc and Fo-Fc maps were initially calculated with FFT from the CCP4 suite and phases from a higher resolution Y81F crystal structure mentioned above (PDB ID:4LHT). B-factors for individual atoms were refined isotropically as well as grouped for TLS refinement and individual coordinates were refined using Phenix.refine. We were concerned about the possibility of model bias due to initial poor 2Fo-Fc density for the cineole ligand. Therefore, we proceeded with two separate trials of refinement by omitting the cineole ligand in one approach and including it in the other. Similar refinement statistics were achieved in either case. Final refinement statistics were achieved through iterative cycles of models improvement in Coot and refinement in Phenix.refine.

Results and Discussion

Substrate Binding

The Y81F mutant does not give a complete low-to-high spin shift even at very high concentrations of cineole. As shown in Fig. 3D there is a about a 50:50 mix of the low-and high-spin forms even at saturation levels of cineole. WT enzyme, on the other hand, displays a single high-spin 392nm peak at micro-molar cineole concentrations (Fig. 3B). It should be noted that previous work reported a 10 fold lower K_s than we obtain 10 (0.7 μ M vs. 5.5 μ M). In these earlier studies a quadratic model was used to fit the binding curve as the simplified model is not accurate when the K_s is less than the enzyme concentration. However, in our case curve fitting using a simplified Michaelis-Menton approach resulted in the same binding constant as a quadratic model. For the Y81F mutant K_s is 125 μ M, about 20 fold larger than WT enzyme (Table 2). As an independent method for estimating substrate binding we utilized isothermal titration calorimetry, (ITC), to provide a spectrally-independent K_D . ITC yields K_D values of 11.8 μ M for WT (Fig. 3A) and 161 μ M for Y81F mutant (Fig. 3C) and thus shows a similar trend to spectrally determined K_s values (inset Figs. 3B, 3D and Table 2).

The ITC results also show that in the WT enyzme, substrate binding is enthalpically unfavorable by 7 kcal mole⁻¹ and thus is entropically driven. The enthalpy and entropy contributions show a similar relationship in the Y81F and N242A mutants. Substrate-free P450 active sites have been shown to be highly solvated^{1,7,37} and the enthalpic penalty probably results from breaking water-water and water-protein hydrogen bonds upon substrate binding. The positive T S term supports evidence of a conformational change that increases solvent entropy by burying exposed hydrophobic residues upon substrate binding as suggested previously for ITC analysis of CYP130 ligand binding.³⁸

The N242A mutant exhibits a very slight low-to-high-spin transition and was too small to confidently determine a K_s using UV-visible difference spectroscopy. ITC gives a $K_D=12.6\mu M$, close to the WT value of 11.8 μM (Table 2). The entropy contribution is also close to the WT value while the enthalpy contribution is approximately 1/7 that of WT. It is unlikely that this small difference is enough to account for loss of the cineole ethereal oxygen-Asn242 hydrogen bond. The reduction in enthalpy also makes sense if substrate binding in the N242A mutant does not expel water from the active site as it does in the WT enzyme, since fewer hydrogen bonds would be disrupted upon substrate binding. The

measured G values are -6.7 kcal/mol and -6.8 kcal/mol for the N242A mutant and wild-type enzymes, respectively. This is in agreement with previous theoretical calulations where the N242A mutant results in only a modest change in binding affinity(0.1 to 0.5 kcal/mol). Therefore, our data confirms that the N242A-cineole hydrogen bond contributes very little to the free energy of substrate binding.

Heme Accessibility, Spin-State and Enzyme Activity

The inability of the mutants to exhibit a full spin-shift could be due to the open state dominating or, alternatively, water remaining coordinated to the heme iron in the closed state. We employed a hydrogen peroxide assay, previously used to measure P450 heme accessibility to small molecules, 15 to probe P450cin solvent accessibility. As shown in Fig. 4, the wild-type heme is much less susceptible to H_2O_2 degradation in the substrate-bound closed state than the substrate-free open state making this method a sensitive probe for the dominant conformation in solution. Y81F is much more susceptible to heme degradation and much higher levels of substrate are required to protect the heme. In sharp contrast, the N242A behaves similarly to WT at 1mM substrate.

Although the Y81F mutant binds substrate more weakly, substrate hydroxylation and coupling efficiency are near WT levels (Fig. S2, Table 2). The N242A mutant, on the other hand, has about 30% WT activity and is over 60% uncoupled in agreement with previously published results. ¹⁰ In P450cam, substrate binding causes a rise in reduction potential such that electron transfer from its redox partner, putidaredoxin, becomes favorable.³⁹ It is likely that in the P450cin N242A mutant, the reduced activity is a function of water coordinating the heme iron giving a large low-spin population. This would result in a lowered redox potential where electron transfer from cindoxin does not occur. This phenomenon would also explain why the N242A mutant binds cineole as strongly as WT but gives very little spin-shift. The crystal structure of a close homolog to P450cam, CYP101D2, 40 shows that the substrate can bind together with water coordinated to the heme iron giving a low-spin complex but the substrate is not oriented correctly for regio- and stereo-selective hydroxylation. In most P450-substrate complexes the carbon atom to be hydroxylated is within 4-5Å of the heme iron, a scenario that is not possible when water is coordinated to the heme. Therefore, there must be some active site adjustments that would allow for simultaneous binding of both water and substrate. We have determined the crystal structures of the N242A and Y81F mutants in order to provide a structural underpinning for these possibilities and to explore how they relate to the active site solvent structure.

Crystal Structures

To obtain crystals of the Y81F mutant, it was necessary to use higher concentrations of substrate (3 mM and 7 mM) compared to WT which readily crystallizes in 1mM cineole. 2mfo-Dfc electron density maps show that the crystals grown in 7mM cineole exhibit greater density than the 3mM structure, underscoring how poorly this mutant binds substrate (Fig. 5C-D). The mutant Phe81 side chain is positioned similarly to the Tyr81 WT side chain but there is a large change in the ordered water network. Water B, normally H-bonded to Tyr81, is clearly missing in the 3mM structure and has poor density in the 7mM structure. Water B is likely important because it provides a bridging H-bond from Tyr81 of the BC loop to the Asp241 residue of the I-helix. At 335ų and 328ų the volumes of the ligand binding cavities determined for the structures in the 3mM and 7mM cineole mutants, respectively, are only slightly expanded compared to the wild type enzyme (300 ų) as calculated by fpocket.²³ However, given our earlier results, lower concentrations of cineole probably result in a more open active-site that has been difficult to crystallize.

Since Asn242 and Tyr81 are tied together in the water-mediated H-bonded network, it was important to better understand the effect of the N242A mutant on the active site water structure. Our earlier 3.05Å structure ¹⁰ did not provide this type of detail but we now have been able to solve the N242A structure to 1.3Å. In addition, at 3.05Å our previous map suggested an ambiguous substrate orientation. Unfortunately, it was not clear enough to interpret precisely how the substrate should be positioned. Our best guess was that multiple orientations were responsible for the observed electron density. However, at much higher resolution it is evident that the substrate is clearly defined and oriented similar to WT P450cin. However, the smaller Ala242 side chain does allow the substrate to rotate slightly, moving closer to the I-helix. The extra room provided by the smaller Ala242 side chain allows four more water molecules into the active site, one of which is 2.3 Å away from the heme iron (Fig. 5B). This water may contribute to the inability of this mutant to produce a significant spin shift in solution. One of the new waters is H-bonded to Gly238 and there is a loss of water B and water C bridged H-bond between Asp241of the I-helix and both the BCloop Tyr81 and the FG-loop H176. The N242A mutant, therefore, breaks a water network that connects the I-helix to the BC and FG-loops. It is also interesting to note that these regions undergo the largest change in the closed/open transition. The increased solvation in the N242A mutant may also be responsible for the uncoupling seen in this enzyme.

The loss of a hydrogen bond between Asn242 and the substrate allows the I-helix to corkscrew so that Asp241 can no longer hydrogen bond with waters B and C. This movement also allows His 176 to retract, pulling the FG loop away from the active site. The net effect is that the distance between Asp241 and Tyr81 is no longer sufficient to entirely close the active site from solvent. In Fig. 6, a surface cutaway representation depicts a new solvent accessible tunnel leading directly to the heme iron as calculated by Caver²². This tunnel traverses a pore created in the N242A mutant. In Fig. 6B we see a clear view to the active site waters in the N242A mutant as opposed to a wild-type enzyme that has a closed active site. In Fig. 6C we can see that the distance between Asp241 and His176 has increased from 4.9 Å to 6.8 Å leaving a pore above the active site. The Asp241 movement is associated with the corkscrewing of the I-helix backbone that also opens up the active site pocket increasing the volume from approximately 300 Å³ to 446 Å³ as calculated by fpocket.²³ The 146 Å³ difference is much larger than the difference in area between the Ala and Asn side chains suggesting that the I-helix movement results in an enlarged ligand binding pocket. An in silico mutation of N242A back to Asn confirms this observation, giving a pocket size of 407 Å³. This suggests that the N242A mutant causes an increase of about 100 Å³ in pocket size that is not due to the void left by removal of the Asn side chain.

In the N242A mutant, the pocket is now bound by the F-helix Thr175 rather than the Tyr81-His176 water bridged pair (Fig. 7). Since uncoupling is often associated with a disruption in the proper proton delivery machinery, the large room and additional solvent very near the $\rm O_2$ binding site in N242A probably accounts for the 60% uncoupling in N242A. Even so, as noted earlier, Asn242 is not as critical for activity as is the Thr252 in P450cam. This is most likely because Thr252 in P450cam directly participates in the H-bonded network required for proper proton delivery to dioxygen while the main role of Asn242 is to hold the substrate in place for regio-selective hydroxylation. 10

Molecular dynamics simulations

Molecular dynamics have provided important insights into solvent channels as well as dynamic properties of active site hydration in P450 enzymes. A1-43 We studied the effect of active site water movement in the WT and N242A mutants by carrying out 75 ns MD simulations. WT enzyme exhibited no water entering the active site pocket throughout the 75 ns simulation while the N242A mutant harbored water in its binding pocket a majority of the time. Given the analysis of the N242A and wild-type crystal structures earlier, it was

tempting to implicate the His176-Asp241 water bridge as the key factor in the differences in solvent accessibility between the two mutants. Analysis of the molecular dynamics simulations, however, paints a different picture.

Evolving solvent accessible channels were tracked during the course of the simulation using CAVER 3.0²² and MDpocket.²⁴ The distance between the His 176 nitrogen and Asp241 carbon does not correlate with the solvent accessible channels formed during the simulation. Rather, it correlates perfectly with the side chain dihedral angles of the His 176 side chain (Fig. 8B). His 176 points towards the active site for almost half of the simulation whereupon it rotates about the C -C bond by over 100 degrees with the two dihedral planes defined by N-C -C and C -C -N. Contrary to our expectations, a change in the His 176 dihedral angle does not cause a solvent accessible channel to form during the course of the simulation. In Fig. 8C the bottleneck radius of the highest scoring channel is plotted as a function of time for N242A in blue, with a yellow trend line, and WT enzyme in black, with a red trend line. The shaded area defines values of tunnel bottleneck radii that are less than 1.4Å, and so are not large enough to allow solvent passage. Both N242A and wild-type enzyme possess channels with bottleneck radii of 1.52 Å and 1.41 Å, respectively, regardless of the His176 dihedral. In the Fig. 8C inset, we can see examples of solvent channels in WT P450cin with H176 in either orientation. It appears that the wild-type enzyme makes subtle adjustments allowing room for a solvent accessible tunnel to form between H176 and D241 regardless of their orientation.

The main difference between the evolving tunnels in WT and the N242A mutant is the tunnel path length. The N242A mutant has an average tunnel length of 15.7 Å, over 3 Å longer than WT with a length of 12.5 Å (Fig. 8D). In Fig. 9 tunnels with bottleneck radii greater than 1.2 Å are visualized for WT and the N242A mutant throughout the simulation. The tunnels form three major clusters: tunnel 1a (blue), 1b (yellow) and tunnel 2 (red) where both tunnel 1b and 2 are offshoots of 1a. In the WT none of these tunnels traversed from the surface to the heme iron. This lack of solvent penetration is due to a narrowing of the active site in the WT enzyme. The tunnels have no problem accessing the N242A heme iron and travel over 3Å further into the active site.

Asn242 undoubtedly acts as a plug to keep the channel from entering the active site. However, its hydrogen bond with the substrate has another function of tightening up the ligand binding pocket. As mentioned earlier, the N242A mutant results in a translation of the I-helix that enlarges the active site pocket by over 100 ų when compared to the wild type as visualized in Fig. 7. This enlargement is far more than can be accounted for by the N242 side chain alone and is maintained over the course of the MD simulations. The increased size of the active site pocket occurs on the I-helix side, probably due to the helix movement discussed earlier. It is important to point out that because P450cin likely undergoes a structural change upon oxygen binding, ^{5,6} we cannot make predictions about solvent accessibility during oxygen activation. However, we can say that the Asn242 residue helps to constrict the active site, keeping water out before catalysis begins.

Conclusions

Although P450 enzyme active sites are predominately hydrophobic, many Fe(III) substrate-bound crystal structures contain ordered waters near the active site. Much work has gone into understanding the role of water, from fundamental structural roles to their participation in proton-relay networks, particularly in P450cam. ^{5,6,44-48} Unfortunately, changes in both active site structure and water during oxygen activation have made these assignments more difficult in cases where an Fe(II)-O₂ complex structure is not available. Here we have found critical roles for 2 water molecules near the Fe(III) P450cin active site. First, the H-bond between water B and Tyr81 is critical to maintaining substrate binding. The Y81F mutant

results in a large increase in solvent accessibility suggesting the predominance of a more open conformation. Thus the removal of just one H-bonding group from the active site water network dramatically decreases substrate binding by shifting the conformational equilibrium to the open state. This observation underscores the delicate energetic balance between the open and closed states. Second, we have also found that the Asn242 residue occurring at a catalytically critical position in other P450s has a role in restricting solvent accessibility to the active site. The N242A mutant disrupts a delicate relationship between the enzyme pocket volume and the ability to exclude excess water, preventing P450cin from converting to the high-spin state. Specifically, N242A, lacking the Asn242-cineole and Asn242-water A H-bonds, causes a shift in the I-helix that disrupts the ordered water network and loosens the ligand binding pocket. This finding may explain why previously published Asn242 mutants show reduced catalytic activity and at least 30% uncoupling. From these results, we conclude that an active site lattice of protein-water H-bonds is important for substrate binding, active site hydration, and controlling the open/close transition all of which are critically important to enzyme function.

Supplementary Material

Refer to Web version on PubMed Central for supplementary material.

Acknowledgments

We would like to thank the University of California, Irvine Department of Chemistry Mass Spectrometry facility and especially Dr. John Greaves and Dr. Beniam Berhane for help in troubleshooting experiments as well as Mass Spec Specialist, Shirin Sorooshian for her dedication in maintaining the instrumentation. YM acknowledges the National Science Foundation for predoctoral fellowship support. SAH was supported by an institutional cancer biology training grant (NIH/NCI T32CA009054). This paper involves research carried out at the Stanford Synchrotron Radiation Laboratory, a national user facility operated by Stanford University on behalf of the U.S. Department of Energy, Office of Basic Energy Sciences. The SSRL Structural Molecular Biology Program is supported by the Department of Energy, Office of Biological and Environmental Research, and by the National Institutes of Health, National Center for Research Resources, Biomedical Technology Program, and the National Institute of General Medical Sciences. We also acknowledge the Advanced Light Source supported by the Director, Office of Science, Office of Basic Energy Sciences, of the U.S. Department of Energy under Contract No. DE-AC02-05CH11231.

References

- Lee YT, Wilson RF, Rupniewski I, Goodin DB. P450cam visits an open conformation in the absence of substrate. Biochemistry. 2010; 49:3412–3419. [PubMed: 20297780]
- 2. Lee YT, Glazer EC, Wilson RF, Stout CD, Goodin DB. Three clusters of conformational states in p450cam reveal a multistep pathway for closing of the substrate access channel. Biochemistry. 2011; 50:693–703. [PubMed: 21171581]
- 3. Stoll S, Lee YT, Zhang M, Wilson RF, Britt RD, Goodin DB. Double electron-electron resonance shows cytochrome P450cam undergoes a conformational change in solution upon binding substrate. Proc Natl Acad Sci U S A. 2012; 109:12888–12893. [PubMed: 22826259]
- Miao Y, Yi Z, Cantrell C, Glass DC, Baudry J, Jain N, Smith JC. Coupled flexibility change in cytochrome P450cam substrate binding determined by neutron scattering, NMR, and molecular dynamics simulation. Biophys J. 2012; 103:2167–2176. [PubMed: 23200050]
- Nagano S, Cupp-Vickery JR, Poulos TL. Crystal structures of the ferrous dioxygen complex of wild-type cytochrome P450eryF and its mutants, A245S and A245T - Investigation of the proton transfer system in P450eryF. J Biol Chem. 2005; 280:22102–22107. [PubMed: 15824115]
- Schlichting I, Berendzen J, Chu K, Stock AM, Maves SA, Benson DE, Sweet RM, Ringe D, Petsko GA, Sligar SG. The catalytic pathway of cytochrome p450cam at atomic resolution. Science. 2000; 287:1615–1622. [PubMed: 10698731]

[†]This work was supported by NIH grant GM33688

7. Madrona Y, Tripathi S, Li H, Poulos TL. Crystal structures of substrate-free and nitrosyl cytochrome P450cin: implications for O(2) activation. Biochemistry. 2012; 51:6623–6631. [PubMed: 22775403]

- 8. Imai M, Shimada H, Watanabe Y, Matsushima-Hibiya Y, Makino R, Koga H, Horiuchi T, Ishimura Y. Uncoupling of the cytochrome P-450cam monooxygenase reaction by a single mutation, threonine-252 to alanine or valine: possible role of the hydroxy amino acid in oxygen activation. Proc Natl Acad Sci U S A. 1989; 86:7823–7827. [PubMed: 2510153]
- 9. Martinis SA, Atkins WM, Stayton PS, Sligar SG. A conserved residue of cytochrome P-450 is involved in heme-oxygen stability and activation. J Am Chem Soc. 1989; 111:9252–9253.
- Meharenna YT, Slessor KE, Cavaignac SM, Poulos TL, De Voss JJ. The critical role of substrateprotein hydrogen bonding in the control of regioselective hydroxylation in p450cin. J Biol Chem. 2008; 283:10804–10812. [PubMed: 18270198]
- Hawkes DB, Slessor KE, Bernhardt PV, De Voss JJ. Cloning, expression and purification of cindoxin, an unusual Fmn-containing cytochrome p450 redox partner. Chembiochem. 2010; 11:1107–1114. [PubMed: 20419722]
- Bergmeyer HU. New values for the molar extinction coefficients of NADH and NADPH for the use in routine laboratories (author's transl). Z Klin Chem Klin Biochem. 1975; 13:507–508.
 [PubMed: 3038]
- Hawkes DB, Adams GW, Burlingame AL, Ortiz de Montellano PR, De Voss JJ. Cytochrome P450cin (CYP176A), Isolation, expression, and characterization. J Biol Chem. 2002; 277:27725–27732. [PubMed: 12016226]
- 14. Pierce MM, Raman CS, Nall BT. Isothermal titration calorimetry of protein-protein interactions. Methods. 1999; 19:213–221. [PubMed: 10527727]
- 15. Sineva EV, Davydov DR. Constrained water access to the active site of cytochrome P450 from the piezophilic bacterium Photobacterium profundum. High Press Res. 2010; 30:466–474. [PubMed: 21475616]
- 16. Humphrey W, Dalke A, Schulten K. VMD: visual molecular dynamics. J Mol Graph. 1996; 14:33–38. 27-38. [PubMed: 8744570]
- Phillips JC, Braun R, Wang W, Gumbart J, Tajkhorshid E, Villa E, Chipot C, Skeel RD, Kale L, Schulten K. Scalable molecular dynamics with NAMD. J Comput Chem. 2005; 26:1781–1802. [PubMed: 16222654]
- 18. Brooks BR, Brooks CL 3rd, Mackerell AD Jr, Nilsson L, Petrella RJ, Roux B, Won Y, Archontis G, Bartels C, Boresch S, Caflisch A, Caves L, Cui Q, Dinner AR, Feig M, Fischer S, Gao J, Hodoscek M, Im W, Kuczera K, Lazaridis T, Ma J, Ovchinnikov V, Paci E, Pastor RW, Post CB, Pu JZ, Schaefer M, Tidor B, Venable RM, Woodcock HL, Wu X, Yang W, York DM, Karplus M. CHARMM: the biomolecular simulation program. J Comput Chem. 2009; 30:1545–1614. [PubMed: 19444816]
- Shahrokh K, Orendt A, Yost GS, Cheatham TE 3rd. Quantum mechanically derived AMBERcompatible heme parameters for various states of the cytochrome P450 catalytic cycle. J Comput Chem. 2012; 33:119–133. [PubMed: 21997754]
- 20. Martyna GJ, Tobias DJ, Klein ML. Constant-Pressure Molecular-Dynamics Algorithms. J Chem Phys. 1994; 101:4177–4189.
- 21. Ryckaert JP, C G, Berendsen HJC. Numerical integration of the Cartesian equations of motion of a system with constraints: molecular dynamics of n-alkanes. J Comp Phys. 1977; 23:15.
- 22. Chovancova E, Pavelka A, Benes P, Strnad O, Brezovsky J, Kozlikova B, Gora A, Sustr V, Klvana M, Medek P, Biedermannova L, Sochor J, Damborsky J. CAVER 3.0: a tool for the analysis of transport pathways in dynamic protein structures. PLoS Comput Biol. 2012; 8:e1002708. [PubMed: 23093919]
- Le Guilloux V, Schmidtke P, Tuffery P. Fpocket: an open source platform for ligand pocket detection. BMC Bioinformatics. 2009; 10:168. [PubMed: 19486540]
- Schmidtke P, Bidon-Chanal A, Luque FJ, Barril X. MDpocket: open-source cavity detection and characterization on molecular dynamics trajectories. Bioinformatics. 2011; 27:3276–3285.
 [PubMed: 21967761]

 Schoneboom JC, Lin H, Reuter N, Thiel W, Cohen S, Ogliaro F, Shaik S. The elusive oxidant species of cytochrome P450 enzymes: characterization by combined quantum mechanical/ molecular mechanical (QM/MM) calculations. J Am Chem Soc. 2002; 124:8142–8151. [PubMed: 12095360]

- Vanommeslaeghe K, Hatcher E, Acharya C, Kundu S, Zhong S, Shim J, Darian E, Guvench O, Lopes P, Vorobyov I, Mackerell AD Jr. CHARMM general force field: A force field for drug-like molecules compatible with the CHARMM all-atom additive biological force fields. J Comput Chem. 2010; 31:671–690. [PubMed: 19575467]
- Vanommeslaeghe K, MacKerell AD Jr. Automation of the CHARMM General Force Field (CGenFF) I: bond perception and atom typing. J Chem Inf Model. 2012; 52:3144

 –3154. [PubMed: 23146088]
- Vanommeslaeghe K, Raman EP, MacKerell AD Jr. Automation of the CHARMM General Force Field (CGenFF) II: assignment of bonded parameters and partial atomic charges. J Chem Inf Model. 2012; 52:3155–3168. [PubMed: 23145473]
- 29. Hollingsworth SA, Karplus PA. A fresh look at the Ramachandran plot and the occurrence of standard structures in proteins. Biomol Concepts. 2010; 1:271–283. [PubMed: 21436958]
- 30. Berry EA, Trumpower BL. Simultaneous determination of hemes a, b, and c from pyridine hemochrome spectra. Anal Biochem. 1987; 161:1–15. [PubMed: 3578775]
- 31. Powell, AGWLaHR. Processing Diffraction Data with Mosflm. Evolving Methods for Macromolec Crystallogr. 2007:41–51.
- 32. Kabsch W. Evaluation of Single-Crystal X-Ray-Diffraction Data from a Position-Sensitive Detector. J Appl Crys. 1988; 21:916–924.
- 33. Winn MD, Ballard CC, Cowtan KD, Dodson EJ, Emsley P, Evans PR, Keegan RM, Krissinel EB, Leslie AG, McCoy A, McNicholas SJ, Murshudov GN, Pannu NS, Potterton EA, Powell HR, Read RJ, Vagin A, Wilson KS. Overview of the CCP4 suite and current developments. Acta Crystallogr D Biol Crystallogr. 2011; 67:235–242. [PubMed: 21460441]
- 34. Adams PD, Afonine PV, Bunkoczi G, Chen VB, Davis IW, Echols N, Headd JJ, Hung LW, Kapral GJ, Grosse-Kunstleve RW, McCoy AJ, Moriarty NW, Oeffner R, Read RJ, Richardson DC, Richardson JS, Terwilliger TC, Zwart PH. PHENIX: a comprehensive Python-based system for macromolecular structure solution. Acta Crystallogr D Biol Crystallogr. 2010; 66:213–221. [PubMed: 20124702]
- 35. Emsley P, Cowtan K. Coot: model-building tools for molecular graphics. Acta Crystallogr Sect D. 2004; 60:2126–2132. [PubMed: 15572765]
- 36. Otwinowski Z, Minor W. Processing of X-ray diffraction data collected in oscillation mode. Macromolec Crystallogr. 1997; 276:307–326.
- 37. Mast N, White MA, Bjorkhem I, Johnson EF, Stout CD, Pikuleva IA. Crystal structures of substrate-bound and substrate-free cytochrome P450 46A1, the principal cholesterol hydroxylase in the brain. Proc Natl Acad Sci U S A. 2008; 105:9546–9551. [PubMed: 18621681]
- 38. Ouellet H, Podust LM, de Montellano PR. Mycobacterium tuberculosis CYP130: crystal structure, biophysical characterization, and interactions with antifungal azole drugs. J Biol Chem. 2008; 283:5069–5080. [PubMed: 18089574]
- 39. Sligar SG, Gunsalus IC. Thermodynamic Model of Regulation Modulation of Redox Equilibria in Camphor Monoxygenase. Proceedings of the National Academy of Sciences of the United States of America. 1976; 73:1078–1082. [PubMed: 1063390]
- 40. Yang W, Bell SG, Wang H, Zhou W, Bartlam M, Wong LL, Rao Z. The structure of CYP101D2 unveils a potential path for substrate entry into the active site. Biochem J. 2011; 433:85–93. [PubMed: 20950270]
- 41. Cojocaru V, Winn PJ, Wade RC. The ins and outs of cytochrome P450s. Biochim Biophys Acta. 2007; 1770:390–401. [PubMed: 16920266]
- 42. Hendrychova T, Berka K, Navratilova V, Anzenbacher P, Otyepka M. Dynamics and hydration of the active sites of mammalian cytochromes P450 probed by molecular dynamics simulations. Curr Drug Metab. 2012; 13:177–189. [PubMed: 22208532]
- 43. Rydberg P, Rod TH, Olsen L, Ryde U. Dynamics of water molecules in the active-site cavity of human cytochromes P450. J Phys Chem B. 2007; 111:5445–5457. [PubMed: 17441761]

44. Haines DC, Tomchick DR, Machius M, Peterson JA. Pivotal role of water in the mechanism of P450BM-3. Biochemistry. 2001; 40:13456–13465. [PubMed: 11695892]

- 45. Kumar D, Altun A, Shaikh S, Thiel W. Water as biocatalyst in cytochrome P450. Faraday Discuss. 2011; 148:373–383. discussion 421-341. [PubMed: 21322494]
- 46. Nagano S, Poulos TL. Crystallographic study on the dioxygen complex of wild-type and mutant cytochrome P450cam. Implications for the dioxygen activation mechanism. J Biol Chem. 2005; 280:31659–31663. [PubMed: 15994329]
- 47. Raag R, Martinis SA, Sligar SG, Poulos TL. Crystal structure of the cytochrome P-450CAM active site mutant Thr252Ala. Biochemistry. 1991; 30:11420–11429. [PubMed: 1742281]
- 48. Vidakovic M, Sligar SG, Li H, Poulos TL. Understanding the role of the essential Asp251 in cytochrome p450cam using site-directed mutagenesis, crystallography, and kinetic solvent isotope effect. Biochemistry. 1998; 37:9211–9219. [PubMed: 9649301]
- 49. Slessor KE, Farlow AJ, Cavaignac SM, Stok JE, De Voss JJ. Oxygen activation by P450(cin): Protein and substrate mutagenesis. Arch Biochem Biophys. 2011; 507:154–162. [PubMed: 20851096]

Abbreviations

CYP cytochrome P450
CO carbon monoxide

Cdx cindoxin CN⁻ cyanide

DEAE diethylaminoethyl cellulose

DEER double electron-electron resonance

DTT dithiothreitol

EPR electron paramagnetic resonance
ENDOR electron nuclear double resonance

IPTG isopropyl -D-1-thiogalactopyranoside

MD molecular dynamics

NADH nicotinamide adenine dinucleotide

ITC isothermal titration calorimetry

NADPH nicotinamide adenine dinucleotide phosphate

NMR nuclear magnetic resonance
PCR polymerase chain reaction
PEG poly(ethylene glycol)

PMSF phenylmethylsulfonyl fluoride RMSD root-mean-square deviation

SDS-PAGE sodium dodecyl sulfate polyacrylamide gel electrophoresis

Tris tris(hydroxymethyl)aminomethane

VMD visual molecular dynamics

WT wild type

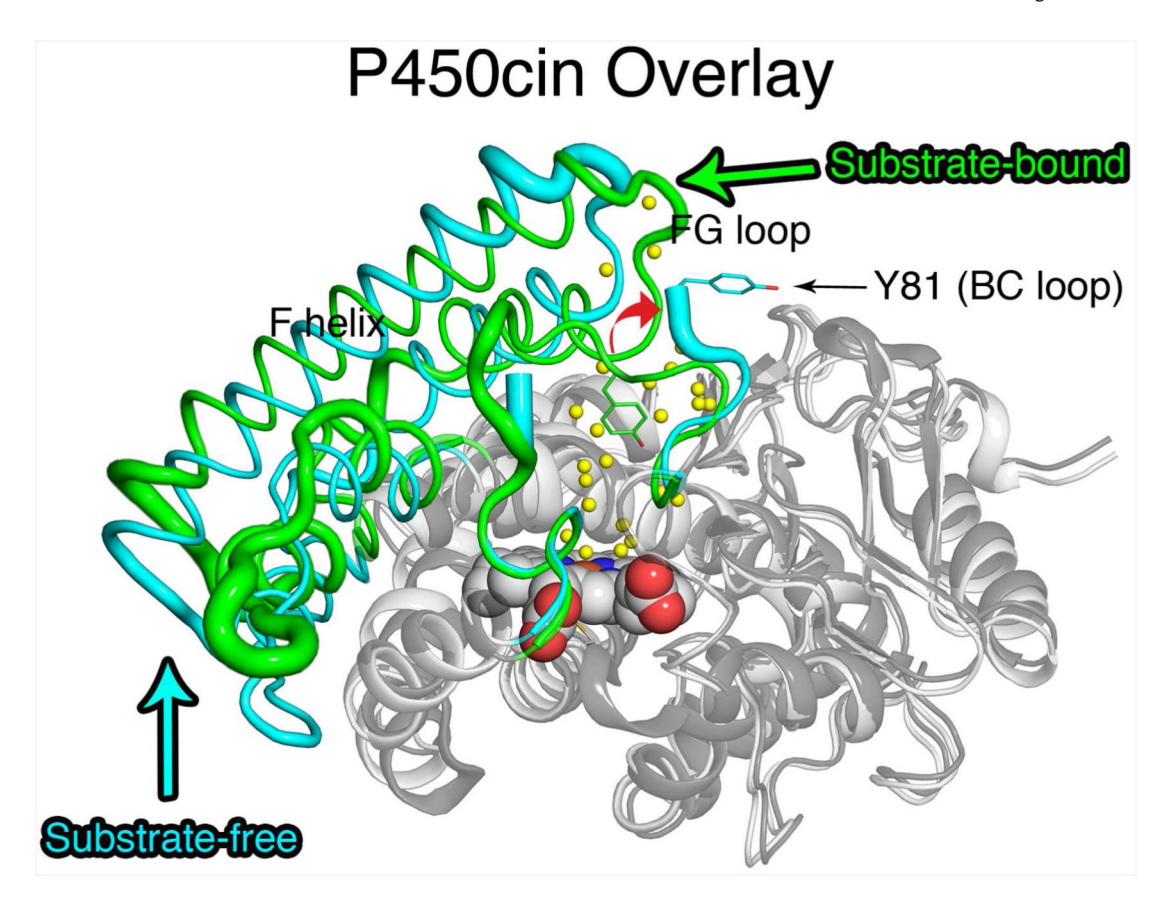


Figure 1. An overlay of substrate-free and substrate-bound P450cin. Regions of greatest C RMSD between the two structures are colored green (substrate-bound) and cyan (substrate-free). The red arrow denotes the direction of movement of Tyr81 from the substrate-bound to substrate-free form.

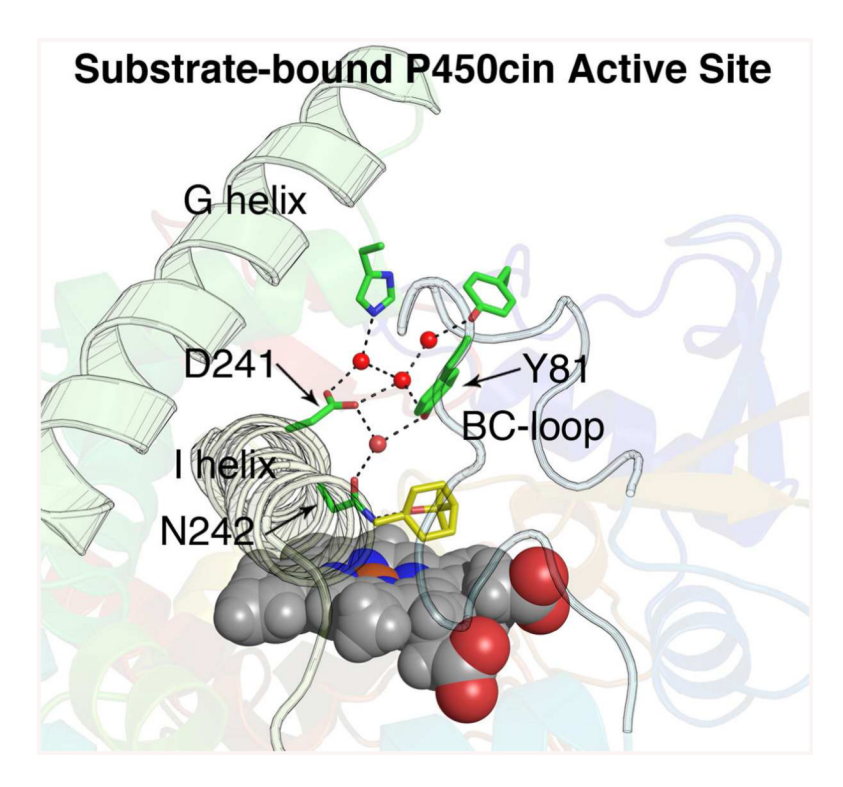


Figure 2. Substrate-bound P450cin active site with key residues colored green, waters colored red and the ligand, cineole, colored yellow. The hydrogen bond network is drawn with black dashes.

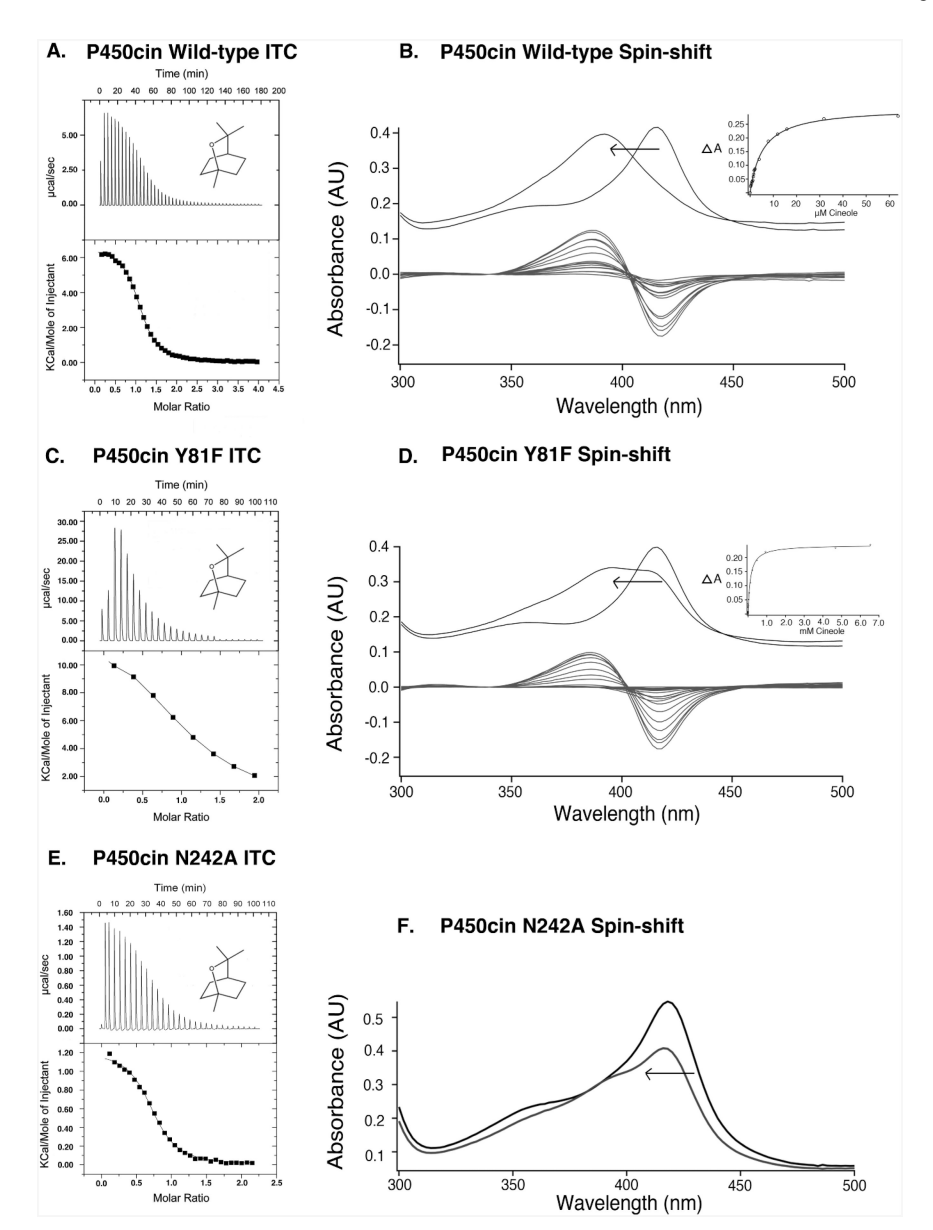


Figure 3. ITC binding isotherms and spectral binding assays for titrating ligand (cineole) into WT, Y81F, and N242A P450cin. Panels A, C and E each consist of the unintegrated heat exchange during each injection at the top and the integrated enthalpy as a function of the molar ratio of cineole to P450cin at the bottom. Curves were fit to a quadratic, one to one binding model to obtain thermodynamic parameters. Panels B, and D depict the spectral binding assays in blue for the WT enzyme and Y81F mutant. The starting and ending spectrum is shown above in grey with the arrow denoting the peak direction upon adding ligand. The difference in high spin (substrate-bound, 393nm) and low-spin (substrate-free, 415nm) is plotted as a function of cineole concentration to give the spectral binding curve shown in the insets. Panel F does not contain a spectral binding curve as the peak to trough difference for the N242A mutant was too small to measure accurately.

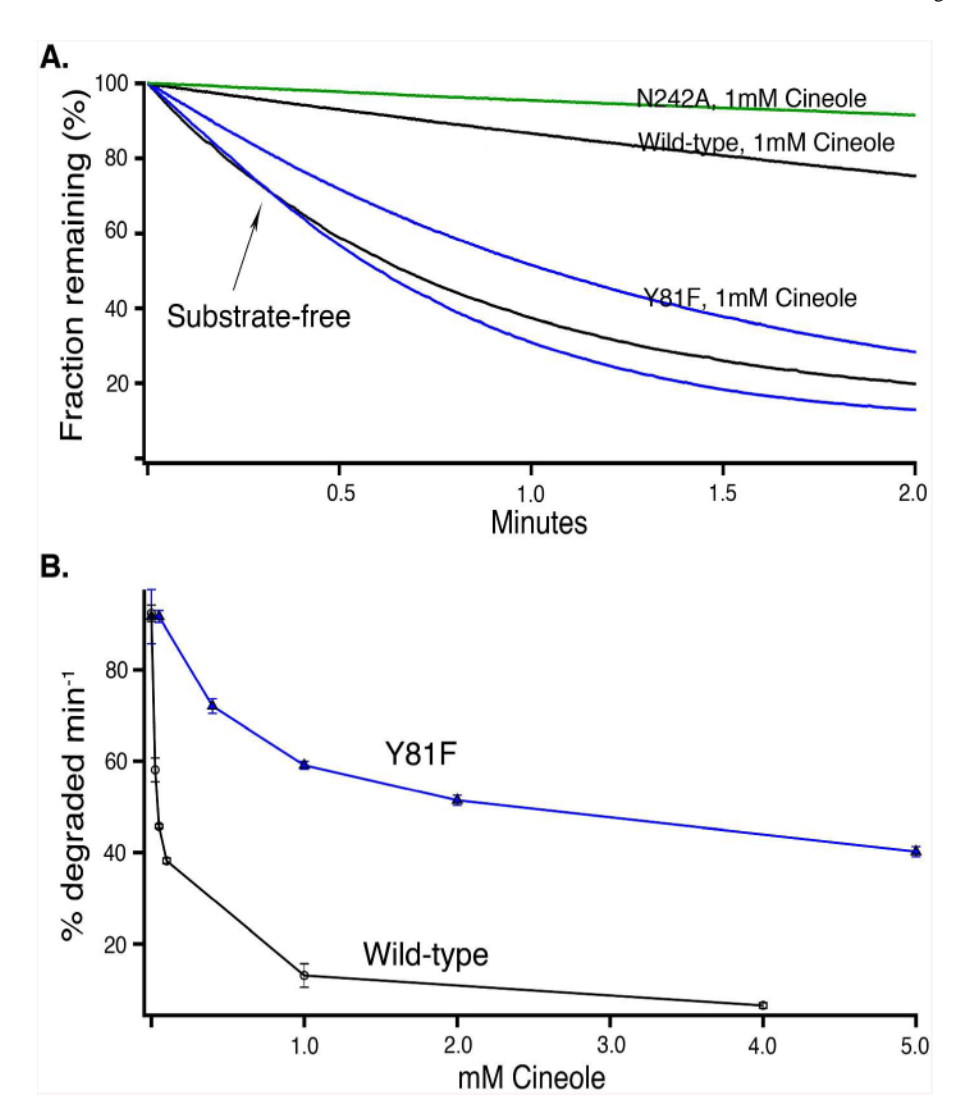


Figure 4. The effect of hydrogen peroxide on heme spectral properties. A) 100mM H_2O_2 was added at time zero followed by monitoring the Soret peak at 392nm for WT and the Y81F mutant. Absorbance at 415nm was monitored for the N242A and substrate-free enzymes. A decrease in absorbance is due to heme destruction by H_2O_2 and provides an estimate of heme accessibility to H_2O_2 . The fraction of the heme remaining for each enzyme was plotted over time. The curve for the N242A mutant is shown in green and those for the Y81F mutant and WT are blue and black respectively. B) The percent heme degraded per minute was determined by plotting the initial slopes of the data from panel A versus increasing concentrations of cineole. The rates for WT and the Y81F mutant are plotted in blue and black, respectively.

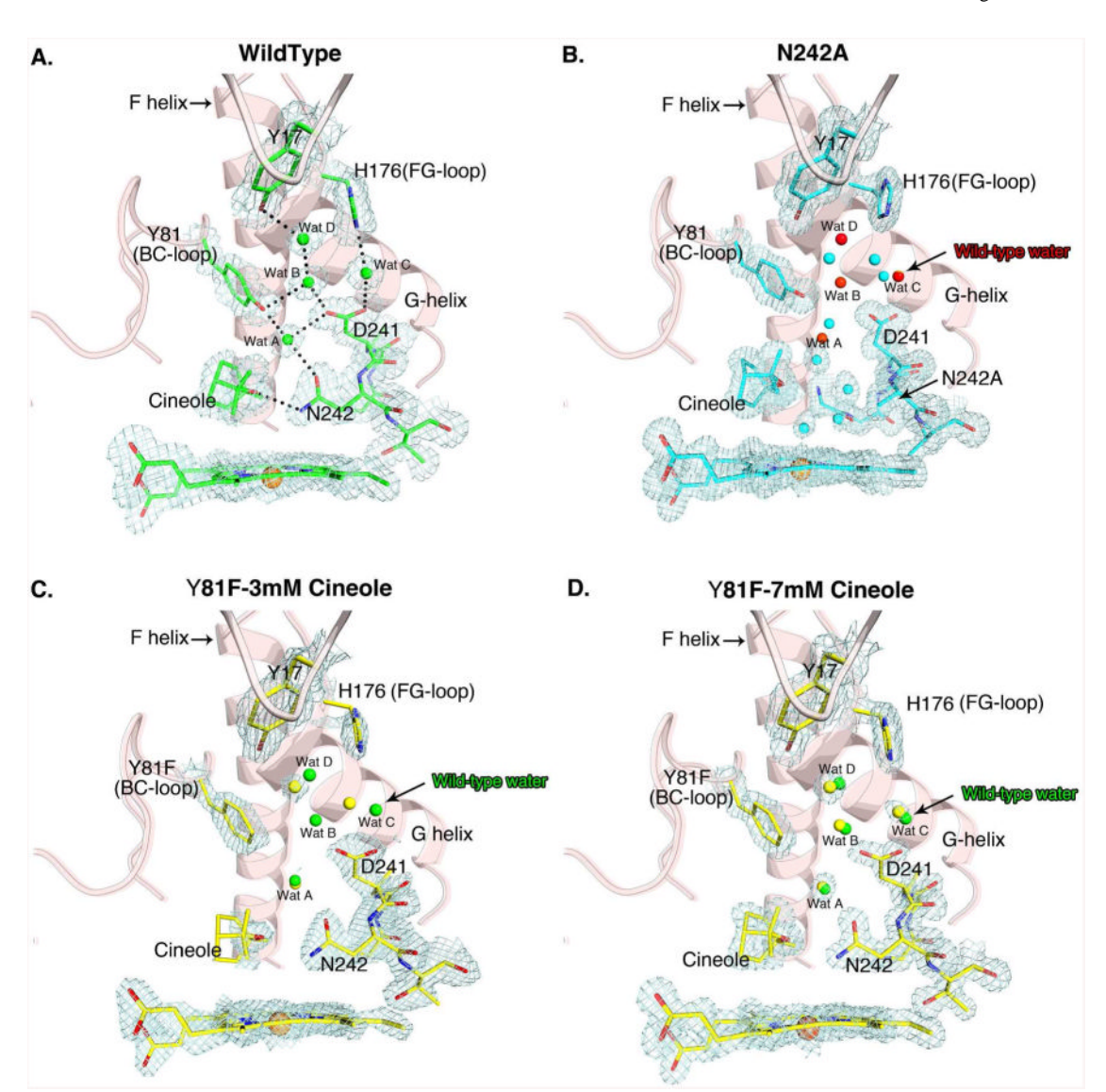
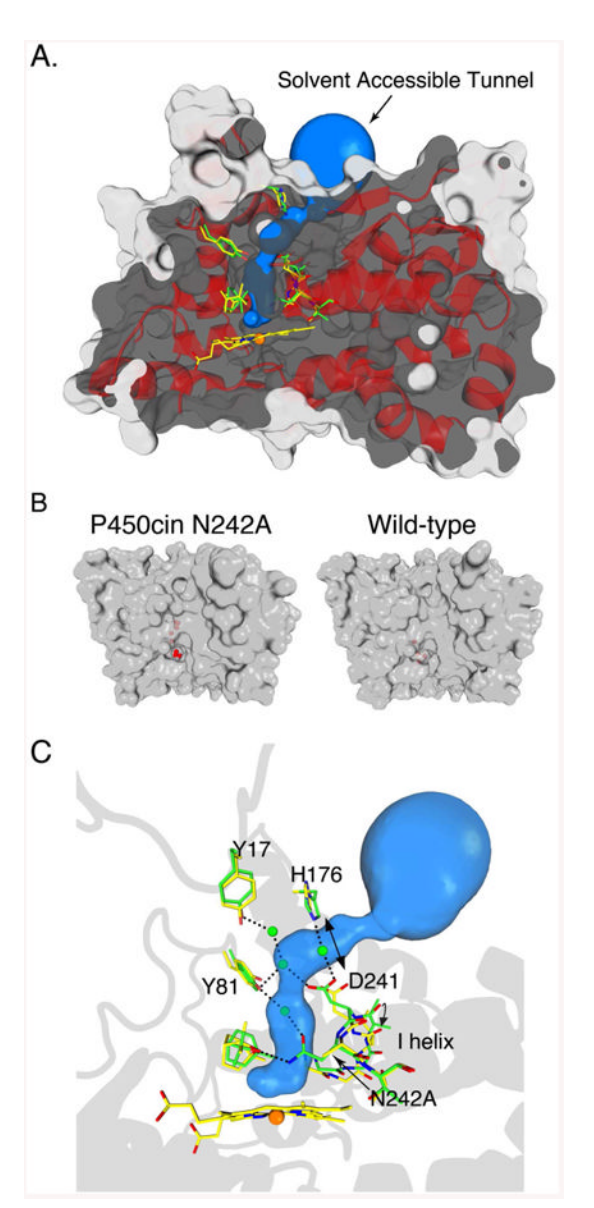


Figure 5.

Active site structures of WT and mutants. 2mfo-Dfc maps were contoured to 1.7 levels and shown for all atoms including water in the active site with the exception of the N242A mutant. For the N242A mutant the 2mfo-Dfc maps were omitted for waters above the cineole ligand in order to clearly compare with the superimposed WT water in Panel C. In Panels B, C and D the WT water structure (red) has been superimposed over the N242A and Y81F active sites. The 2mfo-Dfc map signal is too low for the Y81F mutant to visualize the waters nearest WT waters A and C.



Fiugre 6.

A cross section of the P450cin N242A mutant. A) The surface is colored grey and the backbone is drawn as a red cartoon ribbon. Active site residues are colored yellow and green for N242A and WT P450cin respectively. The solvent accessible tunnel, calculated and visualized by the Pymol Caver 2.0 plugin, is shown in blue. B) Surface representations are depicted for the N242A mutant at left and WT on the right. Active site waters are colored red. C) A close-up of the active site with WT residues shown as green sticks, and superimposed over N242A residues colored yellow.

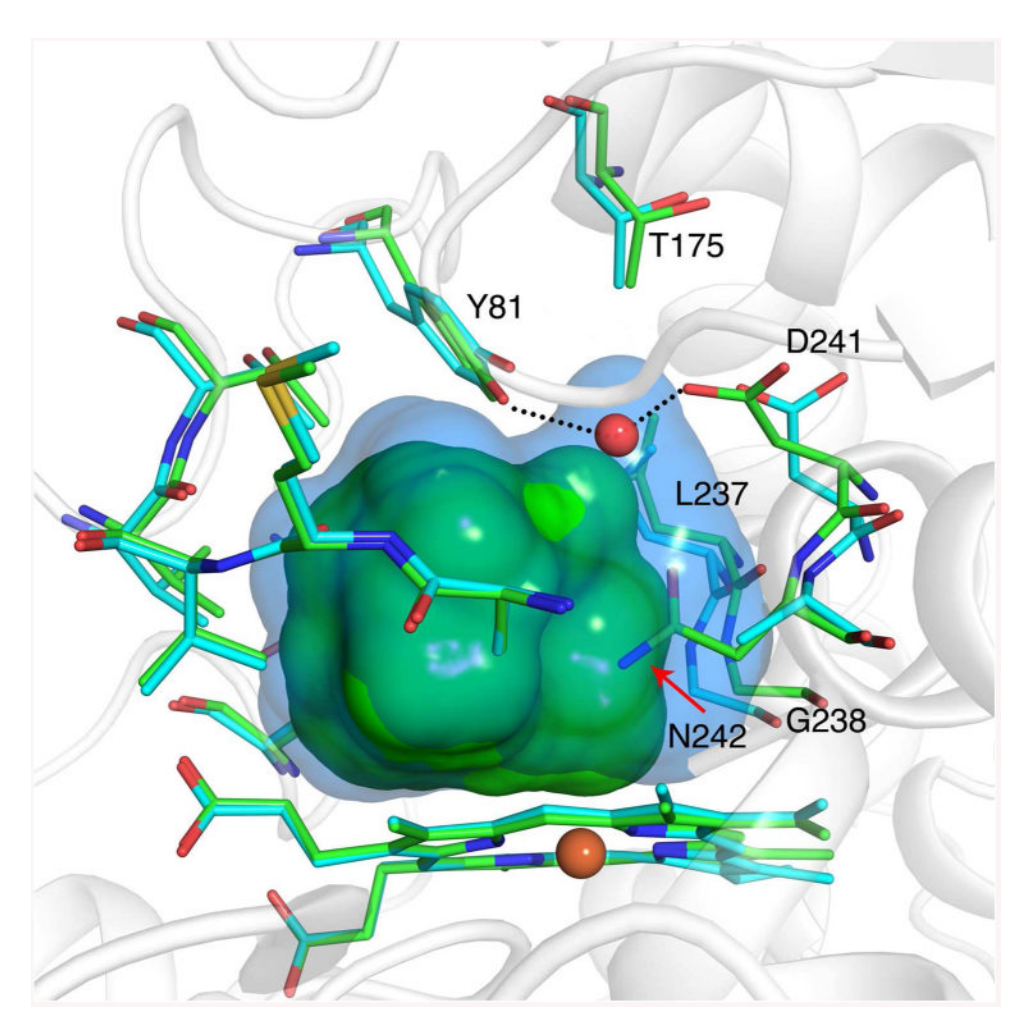


Figure 7. A surface representation of the active site pockets for the wild-type (green) superimposed over the N242A mutant (cyan). The Y81-N241 water bridged H-bond is shown in red with black dashes denoting hydrogen bonding.

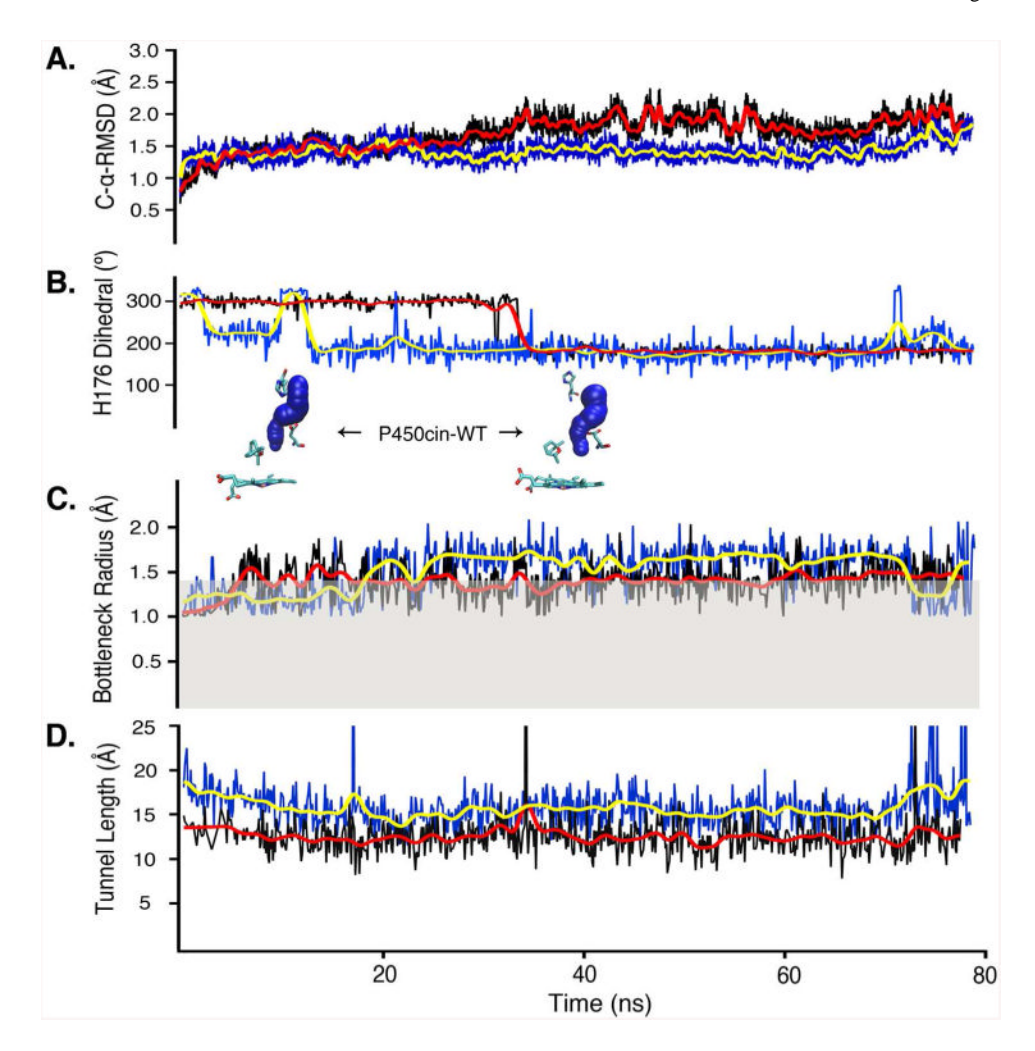


Figure 8.Analysis of molecular dynamics trajectories with WT in black (red trend line) and the N242A mutant in blue (yellow trend line). A) C -RMSD of the WT and mutant enzymes are plotted vs. time. B) The H176 side chain dihedral as defined by the N-C -C and C - C -N planes is plotted over time. C) The average bottleneck radius of tunnels clustered into tunnel 1 were calculated by CAVER3.0 and plotted over the trajectory with a cutoff of 1.0 Å. The grey area represents all bottleneck radii less than 1.4 Å. D) The tunnel length of the solvent accessible channels with bottleneck radii greater than 1.2 Å were plotted over the trajectory.

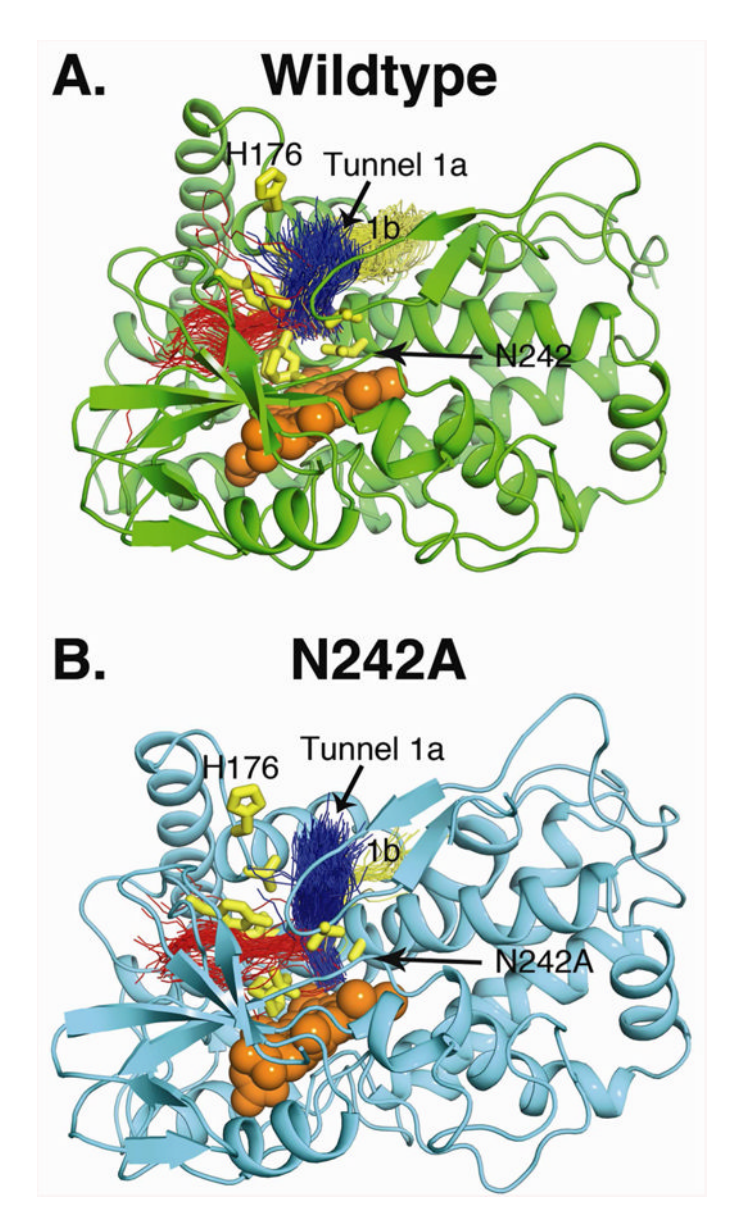


Figure 9.Center lines of individual solvent accessible tunnels are shown as calculated by CAVER3.0 with a bottleneck radius cutoff of 1.2 Å. The top three scoring tunnels after clustering were colored blue, yellow and red respectively. Each line represents a solvent accessible tunnel appearing at some point in the MD simulation.

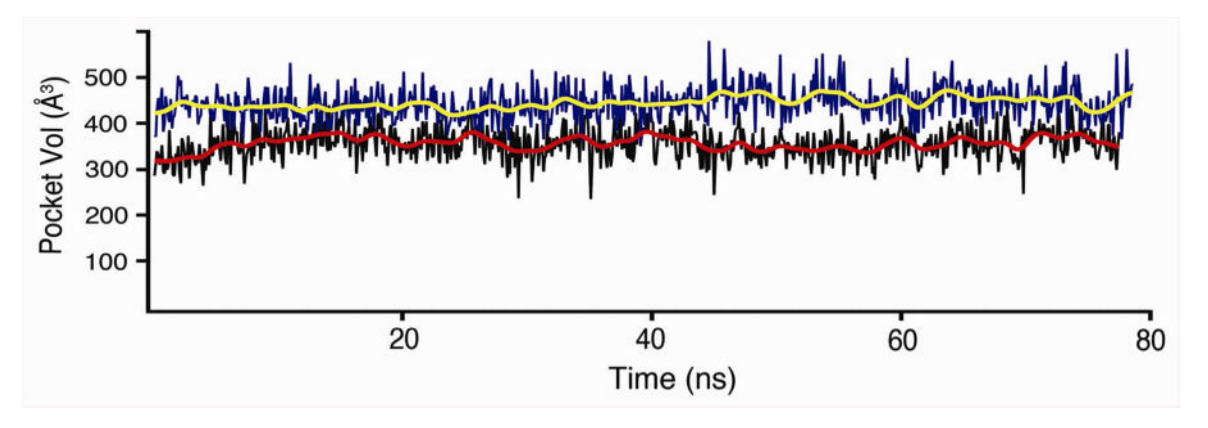


Figure 10. Analysis of the WT and N242A mutant active site pocket volumes calculated by MDpocket over the molecular dynamics trajectories. WT (black with red trend line), and the N242A mutant (blue with yellow trend line) are plotted against time. The analysis shown here was performed every 0.1 nanoseconds over a total simulation time of 75 nanoseconds.

Table 1 Crystallographic Data and Refinement Statistics

Data set	Y81F-3mM Cineole	Y81F-7mM Cineole	N242A
Radiation source	Saturn 944	ALS BL 8.2.1	SSRL BL 9-2
Space group	P212121	P212121	P21
Unit cell dimensions (a,b,c) (Å)	60.46, 103.71, 127.59	68.81, 103.77, 127.71	64.43, 68.17, 103.71 = 95.15°
Resolution Range (Å) (highest shell)	50.34-2.14 (2.22-2.14)	34.75 - 1.37 (1.45 -1.37)	46.68-1.38 (1.45-1.38)
Wavelength (Å)	1.54	1.00	0.98
Total observations	215,793	783,177	483,599
Unique reflections (highest shell)	50,211 (4,797)	185,316(27,034)	181,964 (26,082)
Completeness (%) (highest shell)	98.3(95.5)	97.4 (94.9)	99.5 (98.3)
R _{sym} (highest shell)	.081 (0.257)	.070 (0.472)	.061 (0.354)
<i> (highest shell)</i>	19.7 (4.22)	9.5 (2.0)	16.9 (1.9)
Redundancy (highest shell)	4.3 (2.9)	4.2(3.3)	2.7 (2.2)
B factor, Wilson plot (Å ²)	27.3	15.0	13.7
Unique reflections used in working set refinement	47,577	176,050	172,503
Resolution range (Å) used in refinement	30.9 - 2.14	34.75 - 1.37	43.79 - 1.38
No. of protein atoms fit	6,336	6,336	6,334
No. of heteroatoms fit	143	142	145
No. of waters fit	472	970	1,202
R _{work} %	20.0	16.7	14.2
R _{free} %	26.3	20.7	17.8
RMSD Bond length (Å)	.012	.008	.014
RMSD Bond angle	1.34	1.28	1.58

Madrona et al.

Table 2

Enzymatic and Substrate Binding Data

	kcat min ⁻¹	Product min ⁻¹	% Coupling	$K_{\rm s}\mu{\rm M}$	$K_{\mathrm{D}}\mu\mathrm{M}$	H kcal mole ⁻¹	T S kcal mole ⁻¹	$kcat\ min^{-1} Product\ min^{-1} \%\ Coupling K_s\ \mu M K_D\ \mu M H\ kcal\ mole^{-1} T\ S\ kcal\ mole^{-1} n\ \cdot Binding\ Stochiometry$
Wild-type	253 ± 5.4	248 ± 28.0	8.76	5.5	11.8 ± 0.21	5.5 11.8 ± 0.21 6.90 ± 0.43	13.7 ± 0.43	1.04 ± 0.05
Y81F	166 ± 9.1	178 ± 15.8	105	125.2	161 ± 17.6	125.2 161 ± 17.6 12.8 ± 1.00	18 ± 1.06	1.04 ± 0.04
N242A	79.6 ± 10.6	29.0± 3.0	36.4	-	12.6 ± 1.73	12.6 \pm 1.73	7.89 ± 1.21	0.74 ± 0.08

Page 25